INSTITUTE OF PHYSICS PUBLISHING JOURNAL OF PHYSICS D: APPLIED PHYSICS

J. Phys. D: Appl. Phys. **37** (2004) 2531–2544 PII: S0022-3727(04)77964-4

A unified model of transport phenomena in gas metal arc welding including electrode, arc plasma and molten pool

H G Fan and R Kovacevic[1]

Research Center for Advanced Manufacturing, School of Engineering, 1500 International Parkway, Suite 100, Southern Methodist University, Richardson, TX 75081, USA

E-mail: kovacevi@engr.smu.edu

Received 22 March 2004
Published 1 September 2004
Online at stacks.iop.org/JPhysD/37/2531
doi:10.1088/0022-3727/37/18/009

Abstract

This paper presents a theoretical model for describing globular transfer in gas metal arc welding. The heat and mass transfer in the electrode, arc plasma and molten pool are considered in one unified model. Using the volume of fluid method, the transport phenomena are dynamically studied in the following processes: droplet formation and detachment, droplet flight in arc plasma, impingement of droplets on the molten pool and solidification after the arc extinguishes. The simulation of heat and mass transfer in the arc plasma considers the developing surface profile of the electrode and molten pool and also the effect of the flying droplet inside the arc plasma. Furthermore, the heat inputs to the electrode and the molten pool result from the simulation of the arc plasma. In addition, a He–Ne laser in conjunction with the shadow-graphing technique is used to observe the metal-transfer process. The theoretical predictions and experimental results are shown to be in good agreement.

Nomenclature

B_θ	azimuthal magnetic field
ca, cb	subscripts used at cathode plate, and at the edge of cathode boundary
C_d	drag coefficient
C_p	heat capacity
D_d	droplet diameter
f	droplet transfer frequency
f_L	liquid fraction
F	volume of fluid
g	gravitational acceleration
h	specific enthalpy
h_c	combined heat transfer coefficient at the surface
I	arc current
j_a, j_c	current density at the anode, cathode
j_r, j_z	radial, axial current density
k	thermal conductivity
k_{eff}	effective thermal conductivity
K	drag index in source term
K_B	Boltzmann's constant
K_{max}	maximum drag index
n, s	normal, tangential directions to surface
P	pressure
P_s	surface pressure
Q_{anode}, $Q_{cathode}$	heat source in the anode, cathode regions
Q_c, Q_{cond}, Q_r	convective, conductive and radiative contributions to anode heat flux
r, θ, z	cylindrical coordinate system
R_1, R_2	principal radii of curvature of the surface
R_d	radius of the droplet
S_h, S_w	source term for enthalpy, and axial velocity
S_R	radiation source
t	time
T	temperature
T_{anode}, $T_{cathode}$	anode, cathode temperature
$T_{arc,a}$, $T_{arc,c}$	arc temperature close to anode and cathode

[1] Author to whom any correspondence should be addressed.

T_∞	surrounding temperature
T_l, T_s	liquidus, solidus temperature
T_m	melting temperature
T_r	reference temperature
u, w	radial, axial velocity
U	arc voltage
V_{arc}	velocity of arc plasma
V_c	cathode fall voltage
V_s	tangential velocity along molten pool
V_w	wire feed speed
ΔH	latent heat of fusion

Greek symbols

β	coefficient of thermal expansion
η	arc efficiency
μ	viscosity
μ_0	permittivity of free space
ρ	density
ρ_{arc}	density of arc plasma
τ_s	Marangoni force
σ	electrical conductivity
ϕ	potential
ϕ_w	work function of the anode material
γ	surface tension coefficient
$d\gamma/dT$	temperature gradient of surface tension
ε	emissivity of body surface

1. Introduction

Gas metal arc welding (GMAW) uses an arc between a continuous, consumable filler metal electrode and the weld pool (figure 1). In GMAW, there are various modes of metal transfer including globular, spray, and short-circuit. Globular transfer, where the droplet diameter is larger than the wire diameter, occurs at a low current. The subject of this paper is the transport phenomena of globular transfer. A better understanding of the metal transfer process is important to the quality and productivity of welding.

For droplet formation and detachment, two major analytical models developed are the static force balance theory (SFBT) [1, 2] and the magnetic pinch instability theory (PIT) [2–4]. Four different forces are usually considered: the gravity, arc drag force and electromagnetic force are detaching forces, while the surface tension force is a retaining force. Kim and Eagar [5] have focused on the predication of droplet size using both the SFBT and the PIT. The transition from globular transfer to spray transfer has been discussed using a modified SFBT. From Kim's result, the influence of the electromagnetic force becomes dominate as the current increases. Nemchinsky [6] has developed a steady-state model to describe the equilibrium shape of a pendant droplet, accounting for surface tension and the magnetic pinch force. A simple approximation for the current density distribution in the droplet was used. Simpson and Zhu [7] have developed a one-dimensional model considering the forces acting on the droplet. The model made the first predictions of droplet shape as a function of time. Haidar and Lowke [8] and Haidar [9] have developed a time-dependent two-dimensional model for prediction of droplet formation that includes the arc and predicts the transition from the globular transfer mode to the spray transfer mode. But the model does not simulate the droplet detachment. Further, Choi *et al* [10] have considered the effect of the welding arc under the assumptions of a uniform and linear current density on the droplet surface. However, it has been assumed that the droplets are isothermal. Recently, Wang *et al* [11] have simulated the transition from a globular to a spray transfer mode by assuming a Gaussian current density distribution on the free surface of the drop. Wang *et al* [12] have predicted the geometry of the melting interface, which is in good agreement with the metallographic experiments. However, the model also assumes electrical and thermal fluxes along the droplet and ignores the effect of Marangoni and drag effects on the droplet surface.

In view of the significant effect of the weld pool convection on the microstructure and properties of the resultant weld, numerous investigators have attempted to calculate heat transfer and fluid flow in the weld pool, especially in gas tungsten arc welding (GTAW) [13–17]. Kim *et al* [15] have investigated the effect of various driving forces on heat and mass transfer in a GTA weld pool. In most cases, the fluid flow and heat transfer in the weld pool are controlled by the surface tension force. The surface-active element has been proved to affect the flow pattern in the weld pool and has been used to increase the depth of penetration [16]. Fan and Tsai [17] have simulated the dynamic movement of the molten pool from partial until full penetration. Compared with the GTAW pool, however, the GMAW molten pool has been less studied from both experimental and theoretical aspects due to the interaction between the droplets and base metal. The impingement of molten metal droplets into the weld pool in GMAW affects the shape of the free surface and the convective heat transfer in the weld pool. Tsao and Wu [18] have presented a two-dimensional stationary weld pool convection model for GMAW that assumes the weld pool surface to be flat and takes into account the thermal energy exchange between droplets and the weld pool. Using boundary-fitted coordinates, Kim and Na [19] have presented a three-dimensional quasi-steady model for the moving bead-on-plate GMAW process. The size and profile of the weld pool have been predicted, but the dynamic interaction between the droplet and the weld pool free surface have not been considered. Ushio and Wu [20] have

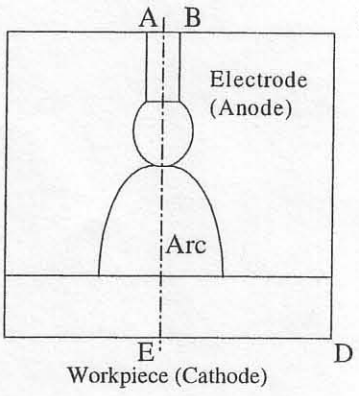

Figure 1. Schematic diagram and calculation domain.

approximated the effect of the droplets on the weld pool as a constant force acting on the weld pool free surface, although, the impingement process is not a continuous process. Fan and Kovacevic [21, 22] have developed a comprehensive model to simulate droplet formation, detachment and impingement on the weld pool. An approximation has been used to get the current density distribution in the droplet. Wang and Tsai [23] have used another non-isothermal model to simulate the droplet impingement on the weld pool surface and the consequent fluid flow in the weld pool. While their paper has focused on the interaction between the droplet and the weld pool, the mechanism of the droplet formation and detachment has not been studied.

For effective usage of the models on the weld pool, accurate information about the welding arc influencing the molten pool is a prerequisite. Modelling the heat transfer and fluid flow in the arc plasma of GTAW has been well-documented [24–28]. Choo *et al* [24] have presented a model of high current arcs with a deformed anode surface; the specified weld pool shapes have been approximated stepwise, and the cathode tip shape has been limited to be flat-ended. In most previous studies on heat transfer and fluid flow in the arc plasma, a current density profile had to be assumed over the surface plane of the cathode [24, 25]. A model without any assumption of the current density at the cathode surface is presented in [26–28]. The distribution of the current density has been calculated with the combined arc–cathode system. Lowke *et al* [28] have developed a simplified unified theory of the GTAW arc and its tungsten electrode. It has been concluded that non-equilibrium sheaths near the electrode can be neglected completely for approximate calculations, provided that optimum grid sizes are chosen near the electrodes. Compared with the GTAW arc plasma, modelling of the GMAW arc plasma has been far less addressed. A two-dimensional steady-state mathematical model has been developed by Jonsson and coworkers [29, 30] to predict the electric potential, temperature and velocity. But the electrode assumes no melting; so, the effects of the electrode shape and droplet on the arc plasma have not been considered. Haidar and Lowke [8, 9] have developed an integrated electrode–arc model: the transport phenomena in the arc plasma have been considered with the effect of droplet formation; but the effect of droplet detachment and the interaction between the arc plasma and the molten pool have not been addressed.

In this paper, a new unified model combining the electrode, arc plasma and workpiece is presented to describe the growth and detachment of molten droplets, the transport and interaction of the molten droplets in the arc plasma, and the interaction between the droplets and the weld pool.

2. Experimental procedures

In GMAW, there are various modes of metal transfer including globular, spray and short-circuit. Lesnewich [31] has showed that the mode of metal transfer depends on many operational variables such as the welding current, electrode extension, electrode diameter and polarity. Johns *et al* [32] have showed a set of particularly well-specified, clear images of the transition from globular to spray transfer. This collection of images is of moving, bead-on-plate GMAW. No attention has been paid to the impact effect of the droplet on the molten pool. The present experiment records the images of stationary GMAW to show the weld pool oscillation triggered by droplets.

In the experiment, an analysis of metal transfer has been performed using high-speed videography with a laser backlighted shadowgraphic method [33]. A power supply (Miller Phoenix™ 456) set in the constant current mode was used to make stationary spot welds on a 4.8-mm thick mild steel plate. The welding was performed under a direct current, electrode positive condition. The electrode used in this experiment was a mild steel welding wire with a diameter of 1.2 mm. The shielding gas used was pure argon. The electrode extension length between the contact tube and the tip of the electrode was 16 mm. Other experimental conditions are given in table 1. The droplet's size (D_d) was measured from the still image on the screen and averaged.

3. Mathematical model

3.1. Governing equations

In order to simplify the mathematical model, the following assumptions have been made:

(1) The welding process is assumed to be axisymmetric.
(2) The gas and liquid flow are assumed to be laminar.
(3) The thermophysical properties of mild steel listed in table 2 are assumed to be constant.
(4) The arc is assumed to be pure argon in local thermodynamic equilibrium (LTE); the plasma properties including enthalpy, specific heat, density, viscosity, radiation and thermal and electrical conductivities are temperature-dependent and are taken from the published data [24]; also, the buoyancy and the heating effect of viscous dissipation are negligible.
(5) The heating effect of the plasma on the travelling droplet is neglected since the superheated droplet temperature does not change significantly in the travelling due to the balance between heat input and metal vaporization.

Table 1. Welding parameters, some determined by measurements on high-speed films.

Welding current, I	160 A	Arc voltage, U	29 V
Wire feed rate, V_w	3.6 m min^{-1}	Droplet diameter, D_d	3.1 mm
Droplet transfer rate	Five drops per second	Gas flow rate	10 l min^{-1}

Table 2. Physical properties of the metal.

Symbol	Value	Symbol	Value
β	10^{-4} K^{-1}	ρ	7200 kg m^{-3}
γ	1.2 N m^{-1}	μ_0	1.26×10^{-6} H m^{-1}
μ	0.006 kg m^{-1} s^{-1}	σ	7.7×10^5 Ω m^{-1}
$d\gamma/dT$	10^{-4} N m^{-1} K^{-1}	ε	0.9
C_p	753 J kg^{-1} K^{-1}	ΔH	2.47×10^5 J kg^{-1}
T_l	1723 K	T_s	1523 K
k	20 W m^{-1} K^{-1}	K_{max}	10^4 s^{-1}

Based on the above assumptions, the governing differential equations used to describe the heat and fluid flow in the droplet and weld pool can be expressed as follows.

Equation of mass continuity:

$$\frac{\partial \rho}{\partial t} + \frac{1}{r}\frac{\partial (r\rho u)}{\partial r} + \frac{\partial \rho w}{\partial z} = 0. \tag{1}$$

Conservation of radial momentum:

$$\frac{\partial}{\partial t}(\rho u) + \frac{1}{r}\frac{\partial}{\partial r}\left(\rho r u u - \mu r \frac{\partial u}{\partial r}\right) + \frac{\partial}{\partial z}\left(\rho u w - \mu \frac{\partial u}{\partial z}\right) = -\frac{\partial P}{\partial r} + \frac{1}{r}\frac{\partial}{\partial r}\left(\mu r \frac{\partial u}{\partial r}\right) - 2\mu\frac{u}{r^2} + \frac{\partial}{\partial z}\left(\mu \frac{\partial w}{\partial r}\right) - j_z B_\theta - K u. \tag{2}$$

Conservation of axial momentum:

$$\frac{\partial}{\partial t}(\rho w) + \frac{1}{r}\frac{\partial}{\partial r}\left(\rho r u w - \mu r \frac{\partial w}{\partial r}\right) + \frac{\partial}{\partial z}\left(\rho w w - \mu \frac{\partial w}{\partial z}\right) = -\frac{\partial P}{\partial z} + \frac{1}{r}\frac{\partial}{\partial r}\left(\mu r \frac{\partial u}{\partial z}\right) + \frac{\partial}{\partial z}\left(\mu \frac{\partial w}{\partial z}\right) - K w + S_w, \tag{3}$$

$$S_w^{arc} = j_r B_\theta, \tag{4}$$

$$S_w^{pool} = j_r B_\theta + \rho g \beta (T - T_r), \tag{5}$$

$$S_w^{drop} = j_r B_\theta - \rho g - \frac{3}{8} C_d \frac{V_{arc}^2 \rho_{arc}}{R_d}. \tag{6}$$

The temperature-dependent drag term, which represents fluid flow in the mushy zone, is incorporated into the momentum equation *via Ku* and *–Kw*, where

$$K = \begin{cases} 0 & T > T_l \text{ or } F = 0, \\ K_{max}\dfrac{T_l - T}{T_l - T_s} & T_s \leqslant T \leqslant T_l, \\ \infty & T < T_s. \end{cases} \tag{7}$$

The right-hand side of equation (6) represents the electromagnetic force, gravity and arc drag force acting on the droplet. Here C_d is the drag coefficient, V_{arc} is the velocity of the arc plasma and ρ_{arc} is the density of arc plasma. The calculation of the arc drag force is detailed in [2].

Conservation of energy:

$$\frac{\partial}{\partial t}(\rho h) + \frac{1}{r}\frac{\partial}{\partial r}\left(\rho r u h - r\frac{k}{C_p}\frac{\partial h}{\partial r}\right) + \frac{\partial}{\partial z}\left(\rho w h - \frac{k}{C_p}\frac{\partial h}{\partial z}\right) = S_h, \tag{8}$$

$$S_h^{drop+pool} = \frac{j_r^2 + j_z^2}{\sigma} - \Delta H \frac{\partial f_L}{\partial t}, \tag{9}$$

$$S_h^{arc} = \frac{j_r^2 + j_z^2}{\sigma} - S_R + \frac{5}{2}\frac{K_B}{e}\left(\frac{j_z}{C_p}\frac{\partial h}{\partial z} + \frac{j_r}{C_p}\frac{\partial h}{\partial r}\right). \tag{10}$$

In the equation (9), Joule-heating is considered. The latent heat of fusion is included by employing the liquid fraction, f_L, which is defined as follows.

$$f_L = \begin{cases} 1 & T > T_l, \\ \dfrac{T - T_s}{T_l - T_s} & T_s \leqslant T \leqslant T_l, \\ 0 & T < T_s, \end{cases} \tag{11}$$

where T_l and T_s are the liquidus and solidus temperatures, respectively.

Equation (10) contains the Joule-heating term, the radiation loss term, S_R and an addition term that represents the transport of electron enthalpy due to the drift of electrons. K_B is the Boltzmann constant, and e is the elementary charge.

Conservation of electrical charge:

In order to obtain the result of electromagnetic force, the electric potential, ϕ, is calculated by solving the equation for current continuity,

$$\frac{1}{r}\frac{\partial}{\partial r}\left(\sigma r \frac{\partial \phi}{\partial r}\right) + \frac{\partial}{\partial z}\left(\sigma \frac{\partial \phi}{\partial z}\right) = 0 \tag{12}$$

and the current density is calculated from Ohm's Law,

$$j_r = -\sigma \frac{\partial \phi}{\partial r}, \qquad j_z = -\sigma \frac{\partial \phi}{\partial z}, \tag{13}$$

while the self-induced azimuthal magnetic field, B_θ, is derived from Ampere's Law.

$$B_\theta = \frac{\mu_0}{r}\int_0^r j_z r \, dr. \tag{14}$$

Tracking of free surfaces:

The moving free surface is tracked using a volume of fluid (VOF) function, F, which represents the VOF in the computational cell. The function F takes the value of 1 for the cell filled with the fluid and becomes 0 for the empty cell that contains an arc plasma. If the cell is located on the free surface, the function F has a value between 0 and 1. The function F is governed by the equation

$$\frac{\partial F}{\partial t} + \frac{1}{r}\frac{\partial}{\partial r}(ruF) + \frac{\partial}{\partial z}(wF) = 0. \tag{15}$$

In addition, there are some numerical techniques for handling the free surface such as the surface pressure due to curvature. These are discussed in detail by Nichols *et al* [34], and will not be reiterated here.

3.2. Boundary conditions

The calculation domain, shown in figure 1, has three regions: an electrode anode region, an arc region and a workpiece cathode region. The cathode and the anode regions consist of solid and liquid phases, and the arc region is pure argon gas. At the axis of symmetry, AE, the following accepted boundary conditions are used: zero radial velocity (u) at the axis, and zero gradients of all other variable conditions normal to the axis.

The electrical potential equation is solved in the integrated anode–arc–cathode domain. At the lower surface of the anode (DE), the electrical potential is assumed to be constant. $\partial\phi/\partial r = 0$ has been set on CD and $\partial\phi/\partial z = 0$ has been set on BC to represent the condition that no current flow crosses this boundary. Over the anode cross-section (AB) a uniform current density of $j_0 = -\sigma(\partial\phi/\partial z)$ is assumed, defined as the input current divided by the area of anode cross-section ($j_0 = I/(\pi R_d^2)$).

For the energy equation, the boundary condition for surface AB is set to be the room temperature. The boundary

conditions for the surfaces without heat input (BC, CD and DE) are expressed as

$$-k\frac{\partial T}{\partial n} = h_c(T - T_\infty), \tag{16}$$

where h_c is a combined heat-transfer coefficient for the radiative and convective boundary expressed in the following equation (15):

$$h_c = 24.1 \times 10^{-4}\varepsilon T^{1.61}. \tag{17}$$

For the calculations of the radial and axial velocities, no-slip conditions are set along solid interfaces. The velocity of the electrode along AB is taken as the wire feed rate, and the velocity of the gas along BC is taken as the gas flow rate. Along surface CD, zero gradients are assumed for the radial and axial velocities for the gas flow. The liquid region is isolated from the gas region by assuming a free boundary surface at the liquid–gas interface. At the free surface, the surface-tension pressure (P_s) can be expressed by

$$P_s = \gamma\left(\frac{1}{R_1} + \frac{1}{R_2}\right), \tag{18}$$

where γ is the surface-tension coefficient and R_1 and R_2 are the principal radii of the curvature of the surface. The Marangoni force due to the variation of the surface-tension coefficient with temperature is described by

$$\tau_s = \mu\frac{\partial V_s}{\partial n} = \frac{d\gamma}{dT}\frac{\partial T}{\partial s}. \tag{19}$$

The surface-tension pressure and the Marangoni force are included by adding source terms to the momentum equation. The method is detailed in [35], which is called the continuum surface force model. For a planar surface, P_s is equal to zero and the surface-tension effects are only due to the Marangoni force. For a curved surface, the two surface-tension effects act simultaneously. In addition, the gas velocities are assumed to be zero along the metal surface. This assumption is based on the approximation that the velocities of the metal are negligible relative to the gas velocity. The momentum transfer from the gas to the liquid is also neglected since the density difference is also big.

3.3. Energy source terms

Between the arc column and electrode surface, there is a thin transition layer in which steep gradients of arc parameters occur. It was assumed that the thickness of the cathode and anode boundary layer is of the order of 0.1 mm [29, 30]. It is known that the cathode layer is thinner than the anode one. However, the calculated results were not sensitive to this assumption for the high current arcs considered in this study [29, 30].

3.3.1. Anode. The electrical energy is mainly transferred to the plasma through Joule heating. The effect of Joule heating is accounted for in the equation for the conservation of thermal energy.

The heat loss in the arc at the anode boundary is mainly due to the Thompson effect (transport of enthalpy due to electron drift) and the effect of conduction. This heat loss is represented by the following expression:

$$Q_{anode} = \frac{k_{eff}(T_{arc,a} - T_{anode})}{\delta} + j_\alpha\phi_w + \frac{5K_B}{2e}j_\alpha(T_{arc,a} - T_{anode}). \tag{20}$$

The first term on the right-hand side is the contribution due to thermal conduction from the plasma to the anode; the second term represents the electron heating associated with the work function of the anode material (ϕ_w); the last term accounts for the thermal energy carried by the electrons into the anode. Here $T_{arc,a}$ is the arc temperature at a distance of 0.1 mm away from the anode; T_{anode} is the anode temperature; and k_{eff} is the effective thermal conductivity at the arc–anode interface, which is the harmonic mean of the thermal conductivities of the arc plasma and anode. j_α is approximated to be the square root of j_r^2 and j_z^2, which are calculated in equation (13). Q_{anode} is also used as the heat input from the arc plasma to the anode (electrode).

3.3.2. Cathode. The energy used to ionize the plasma in the cathode boundary layer, $Q_{cathode}$, is expressed after Szekely and coworkers [24] as

$$Q_{cathode} = |J_c|V_c. \tag{21}$$

Here, $Q_{cathode}$ is a positive energy source supplied to the arc column at the cathode boundary layer and V_c is the cathode fall voltage. In GMAW of iron the cathode is non-thermionic. The physics of the cathode fall region and the thermal balance at a non-thermionic cathode are not very well understood. The following expression is used for the cathode fall voltage following Jonsson and co-workers [29, 30]:

$$V_c = \frac{5k_b}{2e}(T_{arc,c} - T_{cathode}) \tag{22}$$

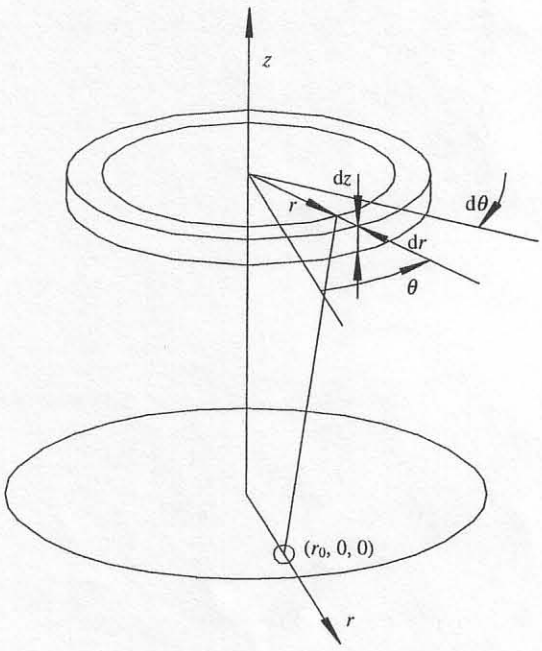

Figure 2. Geometric configuration for calculating radiative heat flux from arc plasma to base plate.

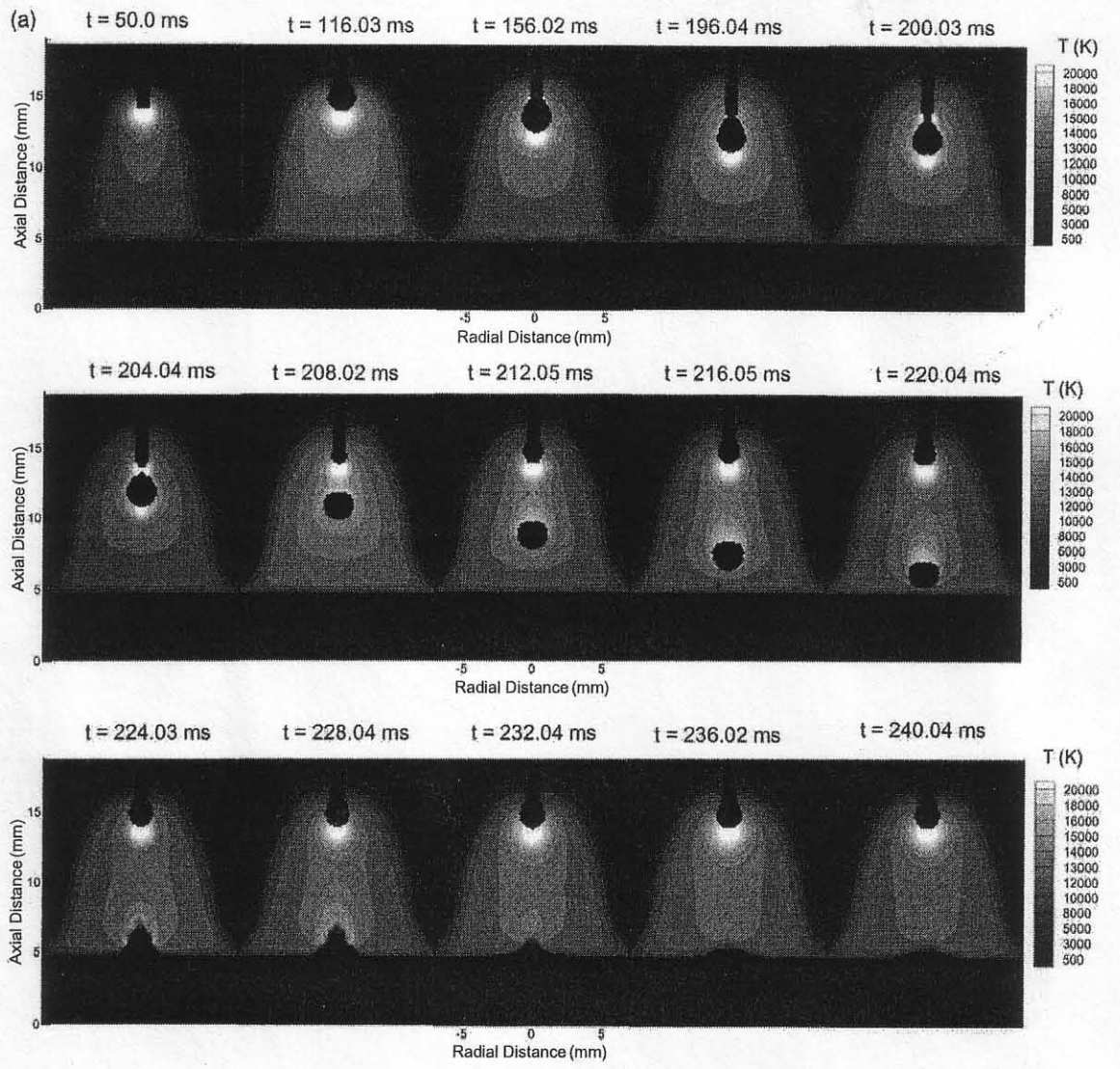

Figure 3. (*a*) Temperature distribution of arc plasma in the process of the formation and impingement of the first droplet on the substrate. (*b*) Velocity distribution of the arc plasma in the process of the formation and impingement of the first droplet on the substrate. (*c*) Current density distribution in the process of the formation and impingement of the first droplet on the substrate.

with T_{cathode} being the temperature of the cathode and $T_{\text{arc,c}}$ the temperature in the arc at a distance of 0.1 mm from the cathode. This will be an approximation, but initial sensitivity calculations [29, 30] have shown that it will not affect the conditions in the arc column or in the anode region, where the highest temperatures exist.

The heat is transferred to the cathode plate by a complex mechanism of convection, radiation and conduction. Each term was calculated using the formula taken from previous work [24, 25]. The convective contribution is written as follows.

$$Q_{\text{c}} = \frac{0.515}{Pr_{\text{ca}}}\left(\frac{\mu_{\text{cb}}\rho_{\text{cb}}}{\mu_{\text{ca}}\rho_{\text{ca}}}\right)^{0.11}\left(\mu_{\text{ca}}\rho_{\text{ca}}\frac{u_{\text{ca}}}{r}\right)^{0.5}(h_{\text{cb}} - h_{\text{ca}}), \tag{23}$$

where the subscripts ca and cb denote the cathode plate and the edge of cathode boundary layer, respectively, and Pr_{ca} is the Prandtl number at the cathode plate. The radiative heat flux at a point r_0 of the base plate was calculated numerically using the following formula [25].

$$Q_{\text{r}} = \int_0^H \int_0^R \int_0^{\pi/2} \frac{S_{\text{R}} r z}{4\pi\{(r - r_0)^2 + z^2 + 4rr_0\sin^2\theta\}^{3/2}} \times \mathrm{d}\theta\,\mathrm{d}r\,\mathrm{d}z, \tag{24}$$

where H and R are the height and radius of the welding arc, respectively. The geometric configuration for calculating equation (22) is shown in figure 2. The heat transfer due to the conduction was similar to that of the anode and is calculated

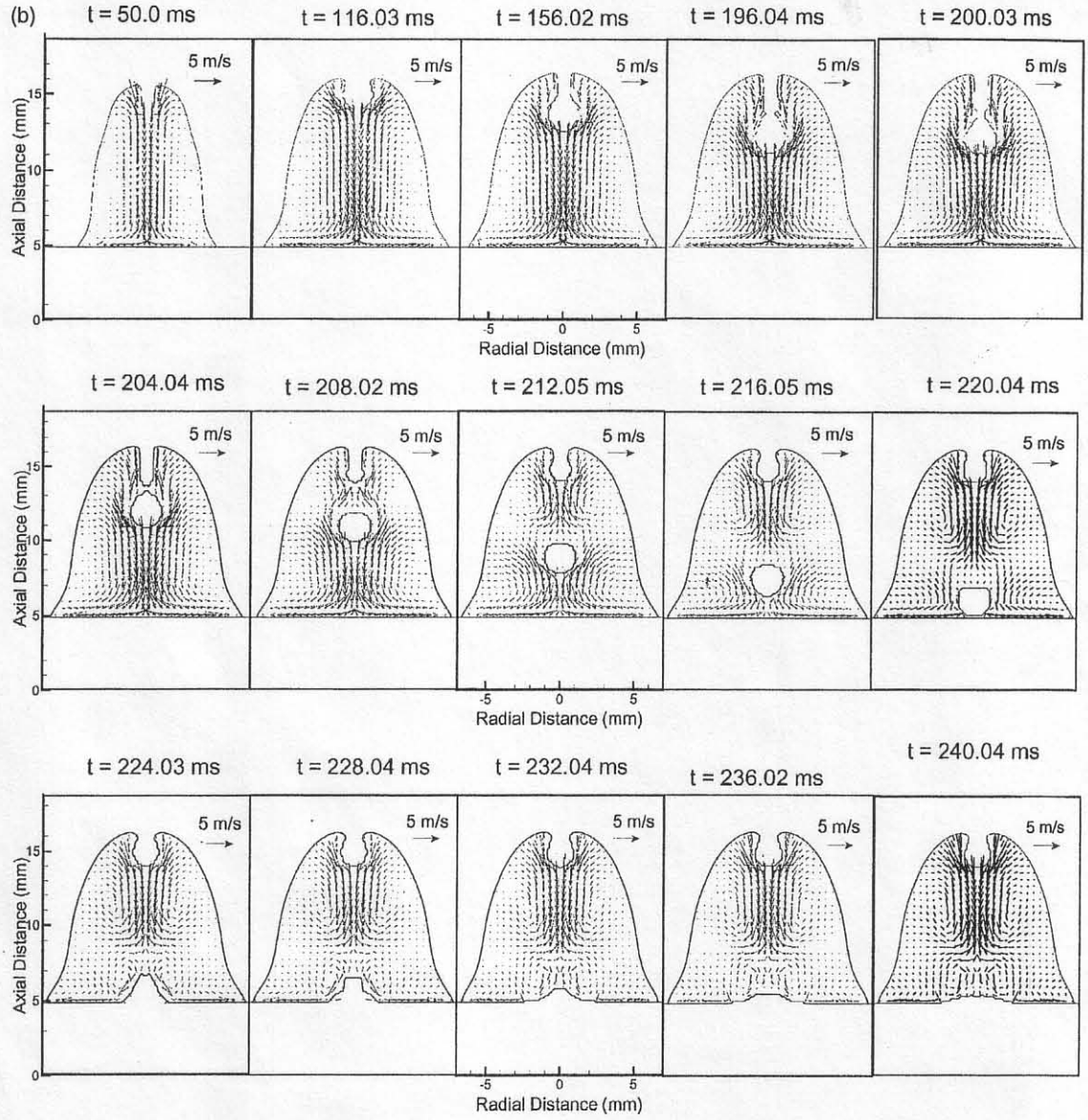

Figure 3. Continued.

as follows.

$$Q_{\text{cond}} = \frac{k_{\text{eff}}(T_{\text{arc,c}} - T_{\text{cathode}})}{\delta}. \tag{25}$$

4. Results and discussion

4.1. Impingement of the droplet on the substrate

Figure 3 depicts the transport phenomena of the welding arc when the droplet is formed, detached and impinged on the substrate. As shown in figure 3(*a*), the mass of the molten wire increases with time. For a current of 160 A, the pendant drop has a classic pear shape. Due to the competition among gravity, surface tension and electromagnetic and arc drag forces, the droplet is elongated and a neck is formed before detachment. Then, the detached droplet is accelerated in the arc plasma by the combined effects of gravity, surface tension and the arc drag force. After the droplet hits the substrate surface, it quickly spreads out on the substrate surface. Figure 3 shows a droplet formation time of approximately 204 ms corresponding to a frequency of around five droplets per second. The calculated average diameter of the droplets is about 2.7 mm, which is slightly smaller than the experimental results shown in figure 4.

Figure 3(*c*) shows the current density distribution for the integrated electrode–arc–workpiece calculation domain. The electrical current leaves the wire and droplet and enters the cathode through the arc space. The current density reaches its greatest value at the neck of the droplet. In order to illustrate the current density distribution in the anode clearly, a large reference length (50 A mm^{-2}) is used before

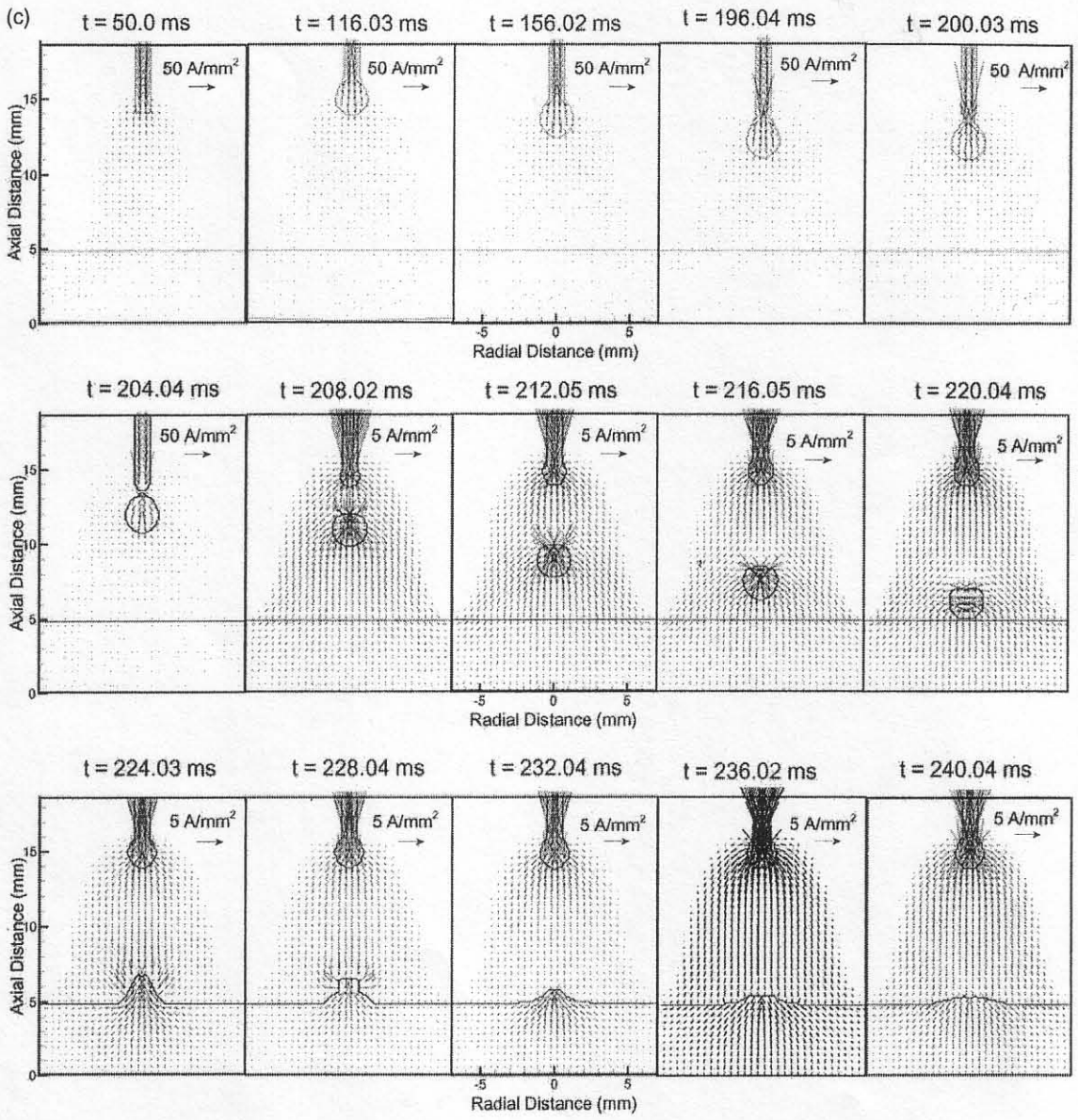

Figure 3. continued.

droplet detachment. After detachment, a small reference length (5 A mm^{-2}) is used to show the current density in the arc plasma and cathode. When the droplet is inside the arc plasma, the current density around the droplet is higher since the metallic droplet has a much higher electrical conductivity than the arc plasma. It is shown that at $t = 224.03$ ms a large part of current enters the anode from the metal protruded into the arc plasma.

Figure 3(a) shows the temperature contours calculated for the arc plasma. In the region of the arc plasma, the typical bell shape of the arc periphery expressed by the isotherm of 5000 K is clearly observed. The maximum temperatures occur on the arc axis near the droplet base because the current density of the arc plasma reaches its biggest value there. In addition, the temperatures around the droplet inside the arc plasma and the temperatures near the neck are relatively higher than their surroundings due to the higher current density. Since the anode and the droplet must be maintained below 3000 K, there are thin boundary layers around them in which steep temperature gradients occur.

The corresponding velocity vectors of the plasma flow in the region where the temperature of arc plasma is above 5000 K are shown in figure 3(b). It is shown that the fluid flows inwards and downwards along the droplet at first and then downwards along the axis of symmetry. Due to the stagnation effect at the cathode, the plasma is then deflected and flows radially outwards along the free surface of the molten pool. The maximum velocity occurs on the arc axis near the

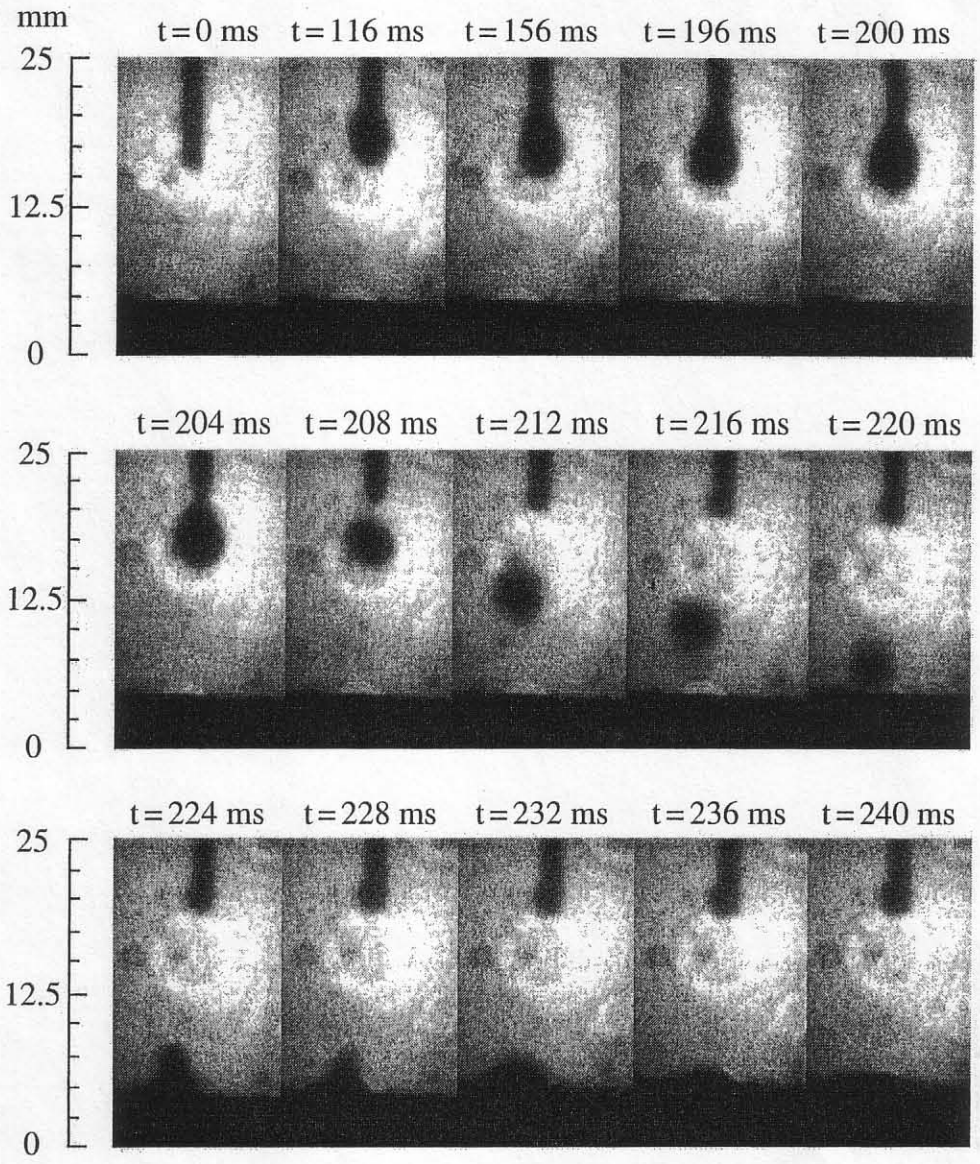

Figure 4. Successive images of the impingement of the first droplet on the substrate.

middle of the arc space. When a droplet is detached and inside the arc plasma, the maximum velocity is decreased since the droplet blocks the acceleration of the arc plasma. The flow of the arc plasma has to go around the droplet. After droplet impingement, a bifurcated flow pattern appears in the upper and lower parts of the arc plasma.

4.2. The last droplet and subsequent solidification

Around the time of 3 s, the arc is extinguished to observe the impact of the last droplet and subsequent solidification. As stated above, the current density in the droplet's neck increases sharply because of the decrease in the current-carrying zone, which causes the electromagnetic force acting on the droplet to increase. The velocity near the neck of the drop, shown in figure 5(*b*) ($t = 3000.04$ ms), is much higher due to the sharp increase in the electromagnetic force. It is suggested that the electromagnetic force plays an important role in droplet detachment.

As the droplet impinges the weld pool, there is a mixing of mass, momentum and energy between the droplet and the molten pool. The addition of the molten droplet increases the volume of the weld pool, the impact of the droplet causes a marked indentation in the weld pool and the heat contained in the overheated droplet is transferred into the weld pool.

As shown in figure 5, when the droplet transfers to the pool, it imparts kinetic energy to a region local to the surface, and this kinetic energy is expended in generating a cavity at $t = 3020$ ms. The fluid is accelerated into the cavity, causing the cavity to fill immediately, and a hump that which overpasses

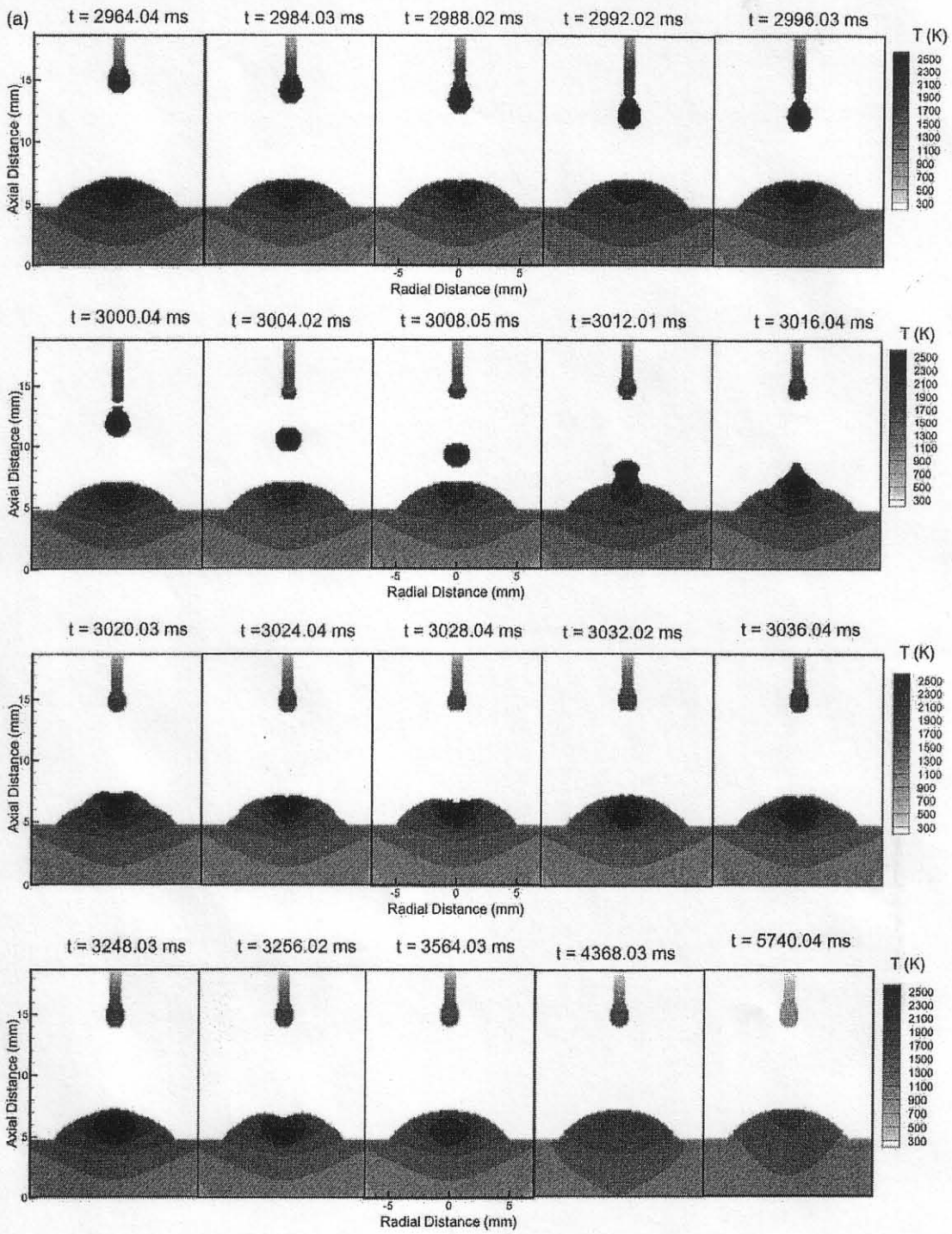

Figure 5. (*a*) Temperature distribution of the molten pool in the process of the formation and impingement of the last droplet and subsequent solidification. (*b*) Velocity distribution of molten pool in the process of the formation, impingement of the last droplet and subsequent solidification.

the equilibrium point is formed at $t = 3024$ ms due to the inertia. That is, part of the kinetic energy has been transformed to potential energy. Under the influence of the hydrostatic, electromagnetic and surface tension forces, the fluid moves downwards at $t = 3028$ ms. Affected by inertia, the downward flow will also pass the equilibrium of the aforementioned forces. Thus, it is observed that the fluid flow moves upwards again at $t = 3036$ ms. Between the impingement of two

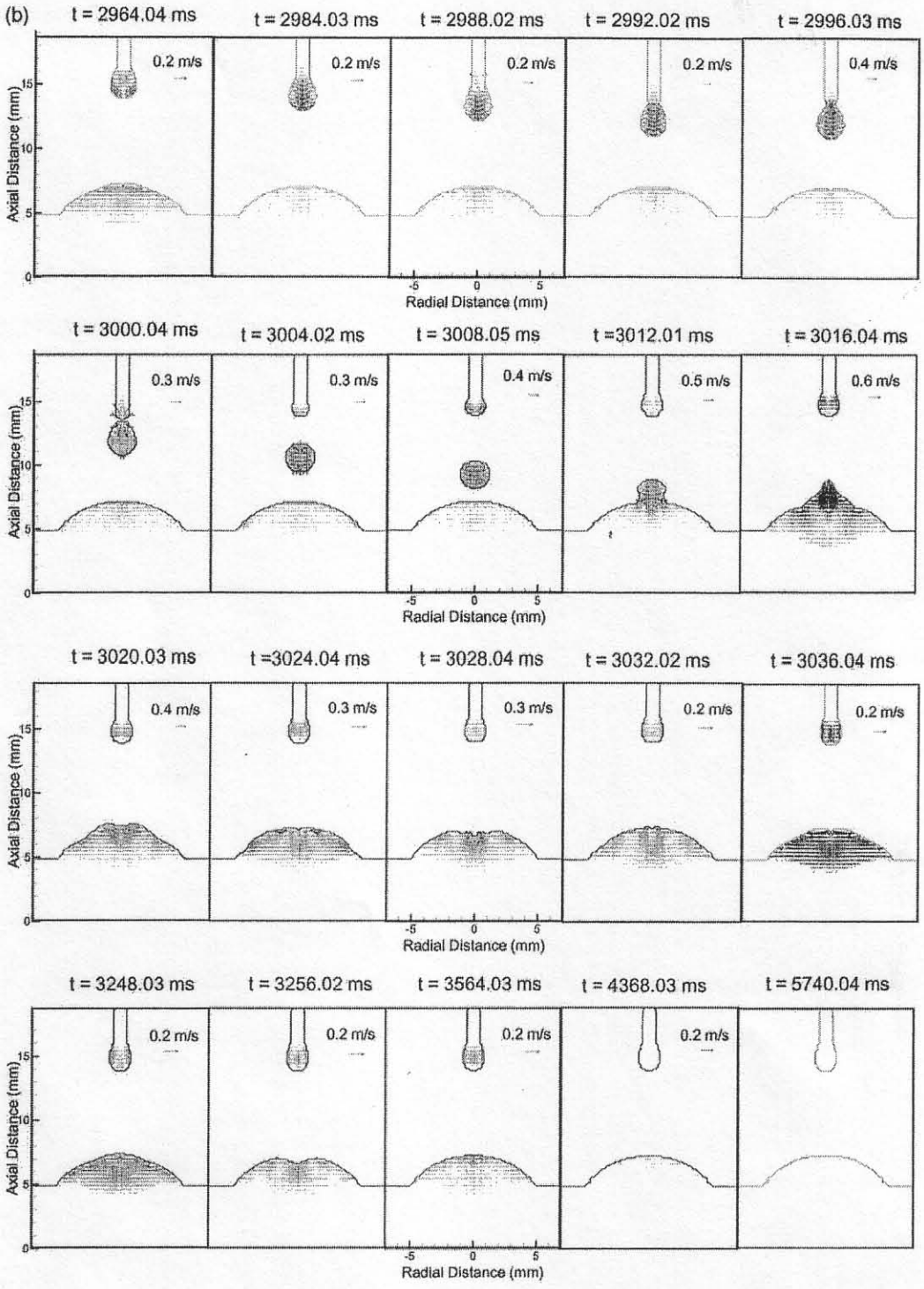

Figure 5. Continued.

consecutive droplets, this loop will continue until equilibrium is achieved. This is called weld pool oscillation.

The added high temperature filler metal is driven downwards due to the momentum of the falling droplets on the pool. Some experiments [36] have concluded that the arc heat influences the depth of penetration only to a limited degree in GMAW. As shown in figure 5(*a*), the high temperature filler metal reaches the position close to the bottom of the weld pool, which suggests that the penetration of the weld pool could be mainly determined by the impingement of droplets. After

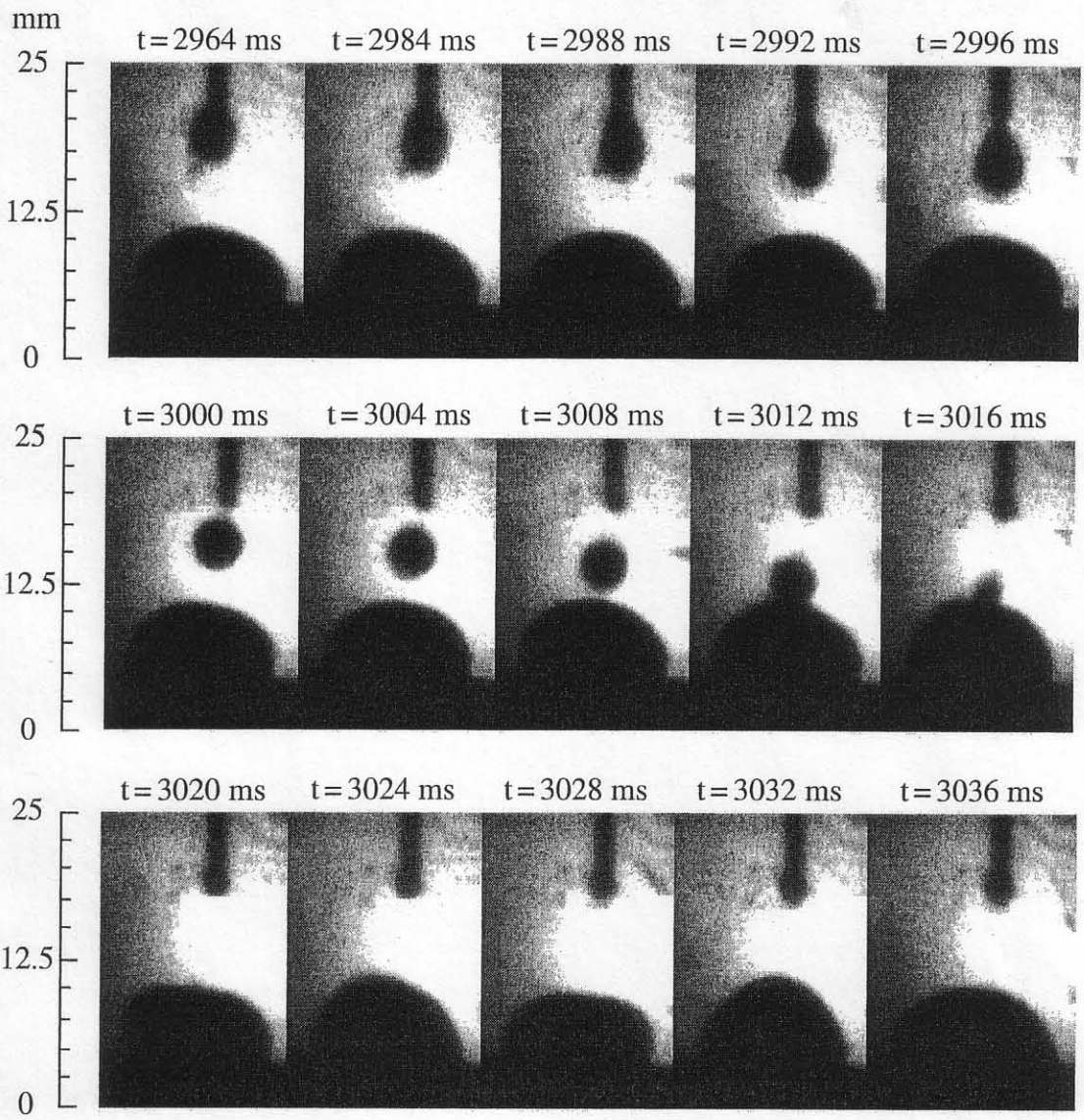

Figure 6. Successive images of the impingement of the last droplet on the molten pool.

the arc is extinguished, the molten droplet and pool become smaller and smaller. The heat loss is mainly from the solid metal; so, the liquid adjacent to the solid–liquid interface solidifies first. The last liquid zone is located in the tip of the droplet and on the top of the weld bead. The solidification of the droplet is completed after about 4 s, while solidification of the molten pool requires about 6 s. The size of the molten pool and the flow pattern are shown in figure 5(*b*). The flow pattern in the weld pool describes the effect of convection on the heat transfer and the weld pool oscillation clearly. It is also shown that the impingement of droplets is a key factor affecting the fluid velocity. The fluid velocity increases significantly after impingement and decreases gradually in the process of solidification.

The experimental images are shown in figure 6. Although the cavity at the centre of the weld pool could not be observed under the current experimental conditions, the obtained images show that the weld pool oscillation could be triggered by the impingement of a droplet, and the amplitude of oscillation is decreased gradually.

The resultant weld bead is shown in figure 7. The actual penetration is less than the predicted results in figure 5(*b*). In actual stationary GMAW, the droplets do not hit the same place every time. In the modelling, we assume the droplets always impact the centre of the molten pool, thus resulting in a deeper penetration. However, the outer shapes of the weld beads are similar since the shape of the weld bead is mainly controlled by surface tension. The locations of impact of the droplets on the workpiece are not a dominant factor affecting the outer shape of the weld bead. In addition, the width of the predicted weld bead is narrower and the height is lower, as compared with the experimental results. The smaller droplet size

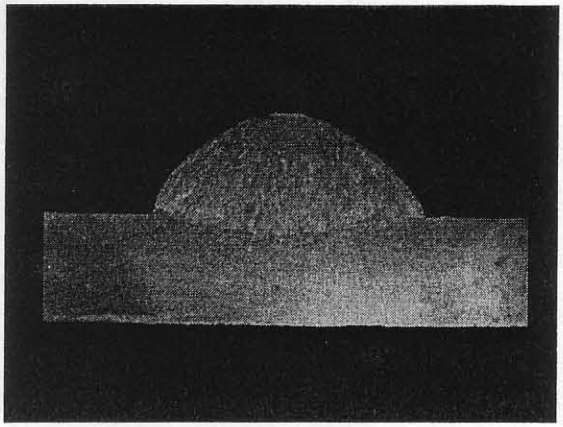

Figure 7. The cross-section of the resultant weld bead.

mentioned before is one affecting factor. Overall, in view of the complexity of the GMAW process, the computational results and experiments are in reasonable agreement. In addition, the model presented could be improved after more theoretical and experimental researches are conducted to understand more about the arc physics in the boundary layers.

5. Summary

A unified model combining the electrode, arc plasma and weld pool is presented to describe the growth and detachment of molten droplets, the transport and interaction of the droplets in the arc plasma, and the interaction between the droplets and the weld pool. The current density distribution is calculated with an integrated electrode–arc–workpiece system, independent of the usual assumptions about current density distributions along the droplet and weld pool surfaces. Two-way interactions between arc–metal interfaces have also been addressed; the simulation of the heat and mass transfer in the arc plasma considers the developing surface profile of an electrode and molten pool and also the effect of a flying droplet inside the arc plasma. Furthermore, the heat inputs to the electrode and the molten pool are obtained from the simulation of the arc plasma. It is shown that the theoretical predications agree well with the experimental results.

Acknowledgments

This work was supported by the National Science Foundation under grant No DMI-0320663 and THECB/ATP grant No 003613-0016-2001, which is gratefully acknowledged.

References

[1] Waszink J H and Graat L H J 1983 Experimental investigation of the forces acting on a drop of weld metal *Weld. J.* **62** 109s–116s

[2] Lancaster J F 1986 *The Physics of Welding* (Oxford: Pergamon)

[3] Allum C J 1985 Metal transfer in arc welding as a varicose instability: I. Varicose instabilities in a current-carrying liquid cylinder with surface charge *J. Phys. D: Appl. Phys.* **18** 1447–68

[4] Allum C J 1985 Metal transfer in arc welding as a varicose instability: II. Development of model for arc welding *J. Phys. D: Appl. Phys.* **18** 1431–46

[5] Kim Y S and Eagar T W 1993 Analysis of metal transfer in gas metal arc welding *Weld. J.* **76** 269s–78s

[6] Nemchinsky V A 1994 Size and shape of the liquid droplet at the molten tip of an arc electrode *J. Phys. D: Appl. Phys.* **27** 1433–42

[7] Simpson S W and Zhu P Y 1995 Formation of molten droplets at a consumable anode in an electric welding arc *J. Phys. D: Appl. Phys.* **28** 1594–600

[8] Haidar J and Lowke J J 1996 Predictions of metal droplet formation in arc welding *J. Phys. D: Appl. Phys.* **29** 2951–60

[9] Haidar J 1998 An analysis of the formation of metal droplets in arc welding *J. Phys. D: Appl. Phys.* **31** 1233–44

[10] Choi S K, Ko S H, Yoo C D and Kim Y S 1998 Dynamic simulation of metal transfer in GMAW: Part 1. Globular and spray transfer modes *Weld. J.* **77** 38s–44s

[11] Wang G, Huang P G and Zhang Y M 2003 Numerical analysis of metal transfer in gas metal arc welding *Metall. Mater. Trans.* B **34** 345–53

[12] Wang F, Hou W K, Hu S J, Kannatey-Asibu E, Schultz W W and Wang P C 2003 Modelling and analysis of metal transfer in gas metal arc welding *J. Phys. D: Appl. Phys.* **36** 1143–52

[13] Zacharia T, David S A, Vitek J M and DebRoy T 1989 Weld pool development during GTA and laser beam welding of type 304 stainless steel: Part I—Theoretical analysis *Weld. J.* **68** 499s–509s

[14] Tsai M C and Kou S 1990 Electromagnetic-force-induced convection in weld pools with a free surface *Weld. J.* **69** 241s–6s

[15] Kim W H, Fan H G and Na S J 1997 Effect of various driving forces on heat and mass transfer in arc welding *Numer. Heat Transfer* **32** (Part A) 633–52

[16] Wang Y and Tsai H L 2001 Modeling of the effects of surface-active elements on flow patterns and weld penetration *Metall. Mater. Trans.* B **32** 145–61

[17] Fan H G and Tsai H L 2001 Heat transfer and fluid flow in a partially or fully penetrated gas tungsten arc welding *Int. J. Heat Mass Transfer* **44** 417–28

[18] Tsao K C and Wu C S 1988 Fluid flow and heat transfer in GMA weld pools *Weld. J.* **67** 70s–5s

[19] Kim J W and Na S J 1994 A study on the three-dimensional analysis of heat and fluid flow in GMAW using boundary-fitted coordinates *Trans. ASME* **116** 78–85

[20] Ushio M and Wu C S 1997 Mathematical modeling of three-dimensional heat and fluid flow in a moving gas metal arc weld pool *Metall. Trans.* B **28** 509–17

[21] Fan H G and Kovacevic R 1998 Dynamic analysis of globular metal transfer in gas metal arc welding—a comparison of numerical and experimental results *J. Phys. D: Appl. Phys.* **31** 2929–41

[22] Fan H G and Kovacevic R 1999 Droplet formation, detachment, and impingement on the molten pool in gas metal arc welding *Metall. Mater. Trans.* B **30** 791–801

[23] Wang Y and Tsai H L 2001 Impingement of filler droplets and weld pool dynamics during gas metal arc welding process *Int. J. Heat Mass Transfer* **44** 2067–80

[24] Choo R T C, Szekely J and Westhoff R C 1992 On the calculation of the free surface temperature of gas tungsten arc weld pools from first principles: Part 1. Modeling the welding arc *Metall. Trans.* B **23** 357–69

[25] Lee S Y and Na S J 1997 Numerical analysis of molten pool convection considering geometric parameters of cathode and anode *Weld. J.* **76** 484s–97s

[26] Zhu P Y, Lowke J J, Morrow R and Haidar J 1995 Prediction of anode temperatures of free burning arcs *J. Phys. D: Appl. Phys.* **28** 1369

[27] Fan H G, Na S J and Shi Y W 1997 Numerical simulation of current density in gas tungsten arc welding including the

influence of cathode *PIME, Part B: J. Eng. Manuf.* **211** 321–7

[28] Lowke J J, Morrow R and Haidar J 1997 A simplified unified theory of arcs and their electrodes *J. Phys. D: Appl. Phys.* **30** 2033–42

[29] Jonsson P G, Eagar T W and Szekely J 1995 Heat and metal transfer in gas metal arc welding using argon and helium *Metall. Mater. Trans.* B **26** 383–95

[30] Jonsson P G, Westhoff R C and Szekey J 1993 Arc characteristics in gas metal arc welding of aluminum using argon as the shielding gas *J. Appl. Phys.* **74** 5997–6006

[31] Lesnewich A 1958 Control of melting rate and metal transfer in gas shielded metal arc welding *Weld. J.* **37** 343s–53s
Lesnewich A 1958 Control of melting rate and metal transfer in gas shielded metal arc welding *Weld. J.* **37** 418s–25s

[32] Johns L A, Eagar T W and Lang J H 1998 Images of a steel electrode in Ar–2%O_2 shielding during constant current gas metal arc welding *Weld. J.* **77** 135s–41s

[33] Rnee S and Kannatey-ashibu E Jr 1992 Observation of metal transfer during gas metal arc welding *Weld. J.* **72** 381s–6s

[34] Nichols B D, Hirt C W and Hotchkiss R S 1980 SOLA-VOF: a solution algorithm for transient fluid flow with multiple free boundaries *Report* LA-8355, Los Alamos Scientific Laboratory

[35] Kothe D B, Mjolsness R Ca and Torrey M D 1991 RIPPLE—a computer program for incompressible flows with free surfaces *Report* LA-12007-MS, Los Alamos Scientific Laboratory

[36] Essers W G and Walter R 1981 Heat transfer and penetration mechanisms with GMA and plasma-GMA welding *Weld. J.* **61** 37s–58s